Soft Matter

PAPER

View Article Online
View Journal | View Issue

Cite this: *Soft Matter*, 2023, **19**, 6458

The cohesive properties and pyrolysis mechanism of an aprotic ionic liquid tetrabutylammonium bis(trifluoromethanesulfonyl)imide†

Shijie Liu,[a] Runhong Wei,[b] Guangjun Ma,[c] Ailin Li,[d] Olaf Conrad[e] and Jiangshui Luo *[a]

Received 11th May 2023,
Accepted 22nd May 2023

DOI: 10.1039/d3sm00614j

rsc.li/soft-matter-journal

As the cohesive properties (such as the enthalpy of sublimation) of solid organic salts (or ionic liquids, ILs) are unmeasurable, a method of their indirect determination is proposed in this paper. For this purpose, the thermogravimetric analysis (TGA) and differential scanning calorimetric analysis (DSC) were carried out over a wide range of temperatures. In this study, the mathematical relationship of the thermodynamic properties between the liquid and solid phases of ILs is established using the Born–Fajans–Haber cycle, in which the sum of the vaporization enthalpy of ILs, melting enthalpy and the enthalpy of solid–solid phase transition is regarded as the sublimation enthalpy of solid organic salts. With this method, the cohesive properties of tetrabutylammonium bis(trifluoromethanesulfonyl)imide ($[N_{4444}][NTf_2]$), which is an aprotic IL, were successfully obtained. Additionally, the difference between the lattice energy and the cohesive energy was employed to quantitatively calculate the charge separation distance of single ion pair (r_{12}) in the gas phase of ionic liquids for the first time, which can serve as a standard methodology to measure the closeness in distance between the anion and the cation in a gas phase ion pair. The pyrolysis mechanism of $[N_{4444}][NTf_2]$ was also explored.

Introduction

Ionic liquids (ILs) are generally defined as compounds entirely composed of ions with a melting point below 100 °C. Benefiting from their structural features and unique physical or chemical properties such as low vapor pressure, tuneable polarity and structure, nonflammability, broad solubility, and high thermal stability, multidisciplinary studies of ILs have been emerging, involving chemistry, materials science, chemical engineering, physics, thermal engineering, computational science, and environmental science (such as catalysis,[1] gas adsorption/desorption,[2] extractants,[3] proton conductors,[4] electrochemistry,[5] thermal energy storage,[6] and heat transfer fluids[7]). Moreover, some fundamental viewpoints are different from the original ones with the understanding of the nature of ILs being deepened. For example, the concept of physicochemical properties of ILs was shifted from non-volatile to principally volatile in the last 15 years.[8] The change in the concept about volatility triggered the research on the quantitative analysis of the volatility of the ILs in the condensed phase. A few experimental methods have been modified to measure the enthalpy of vaporization (ΔH_{vap}) and the vapor pressure (P_{vap}) of both protic and aprotic ILs, such as line-of-sight mass spectrometry (LOSMS),[9a] isothermogravimetric analysis (IGA),[9b] ultraviolet spectroscopy (UV),[9c] quartz crystal microbalance (QCM),[9d] and the traditional Knudsen method,[9e] among which IGA is a relatively simple and efficient method.[9b,10]

ΔH_{vap} reflects molecular interactions in the liquid state and can serve as a foundation for calibrating and validating force fields in molecular dynamics simulations[9] and as an anchoring parameter in *P–V–T* equations for neat ILs. Meanwhile, the enthalpy of sublimation (ΔH_{sub}) can be employed to estimate the strength of molecular interactions in the solid organic salts (*i.e.* crystalline or solidified ILs or ILs in the solid state). The solid organic salts have much lower vapor pressure than the liquid-state ones, while there are few studies on the experimental methods about their ΔH_{sub}. The available few cohesive properties of solid organic salts are calculated by quantum chemical simulation.[11] Nonetheless, they are generally scattered data at

[a] *Lab of Electrolytes and Phase Change Materials, College of Materials Science and Engineering & Engineering Research Center of Alternative Energy Materials & Devices, Ministry of Education, Sichuan University, Chengdu 610065, China. E-mail: Jiangshui.Luo@scu.edu.cn*
[b] *Fujian Ningde Aishuyuncheng New Materials Technology Co., Ltd., Ningde 355200, China*
[c] *Chengdu Weilai Engineering Technology Co., Ltd, No. 366 North Section of Hupan Road, Zhengxing Street, Tianfu New District, Chengdu 610299, China*
[d] *College of Science, Civil Aviation University of China, Tianjin 300300, China*
[e] *Pajarito Powder LLC, 3600 Osuna Rd, Albuquerque, NM 87109, USA*
† Electronic supplementary information (ESI) available. See DOI: https://doi.org/10.1039/d3sm00614j

several temperatures and can hardly reflect their dependence on temperatures because of the massive quantum chemical calculations for a wide temperature range.

Additionally, experimental and computational methods for the volatilization process of ILs have established that the gaseous phase volatilized from aprotic ILs consists of isolated tight neutral ion pairs.[12] The gaseous ion pairs are an intermediate state between the gaseous phase ions and condensed matter of aprotic ILs. Consequently, the energy difference between the cohesive energy and lattice energy of solid organic salts can indicate the potential energy of the gaseous ion pairs. However, the quantitative studies on the gaseous ion pairs are insufficient owing to the data scarcity of cohesive properties. Recently, Červinka *et al.*[11] calculated the values of ΔH_{vap} and ΔH_{sub} of condensed ILs using a combination of quantum chemical calculations and thermal analysis. Specifically, ΔH_{vap} and ΔH_{sub} are associated with enthalpy of fusion (ΔH_{fus}): $\Delta H_{sub} = \Delta H_{fus} + \Delta H_{vap}$. Krossing *et al.*[13] developed a model to predict melting temperatures by using a suitable Born–Fajans–Haber cycle that was closed by the lattice Gibbs energy and the solvation Gibbs energies of the constituent ions in the molten salts.

In this paper, the cohesive properties of solid organic salts are investigated using Born–Fajans–Haber cycles, in which the enthalpy of sublimation is the sum of the enthalpy of solid–solid transitions (if there are), the enthalpy of melting and the enthalpy of vaporization. The basic thermodynamic parameters can be measured by thermogravimetric analyzer (TGA) and differential scanning calorimetry (DSC). In contrast to the complex quantum chemical simulation, the cohesive properties of solid organic salts can be obtained by calculating the sum of the measured data. Thus, the reported method avoids the large time consumed for geometry optimization, thermodynamic equilibria, and energy calculations. The enthalpy of sublimation and the cohesive energy of tetrabutylammonium bis(trifluoromethanesulfonyl)imide ($[N_{4444}][NTf_2]$) as a model solid organic salt were determined for the first time by this method. In addition, the cohesive properties of 1-ethyl-3-methylimidazolium bis(trifluoromethanesulfonyl)imide ($[C_2mim][NTf_2]$) and 1-butyl-3-methylimidazolium bis(trifluoromethanesulfonyl)imide ($[C_4mim][NTf_2]$) were determined to testify the method's universality for ILs. Moreover, the energy difference between the cohesive energy and lattice energy of solid organic salts is adopted in this study to estimate the average charge separation in the single gaseous ion pair (r_{12}) by the Born–Mayer equation based on the calculated cohesive energy of solid organic salts. The parameter r_{12} can reflect the degree of contact between the anion and the cation in the gaseous ion pair.

Furthermore, the thermal stability of ILs is a crucial property that allows for long-term and safe applications at high temperatures,[14] such as thermal energy storage materials and heat transfer fluids. These properties can provide useful information about the maximum operating temperatures and the pyrolysis half-lives. TGA techniques were thus also employed to examine the pyrolysis kinetics of $[N_{4444}][NTf_2]$. The kinetic parameters during the pyrolysis were calculated with differential and integral methods.

Therefore, the specific objectives of this work are comprised of: (i) an assessment of cohesive properties of $[N_{4444}][NTf_2]$ in both the solid and liquid states, and (ii) a systematic investigation of the pyrolysis mechanism of $[N_{4444}][NTf_2]$.

Experimental

Materials

Tetrabutylammonium bis(trifluoromethanesulfonyl)imide (abbreviated as $[N_{4444}][NTf_2]$; CAS number: 210230-40-3; molecular weight (M_W): 522.61 g mol^{-1}; purity: ≥99%) was purchased from Lanzhou Greenchem ILs, LICP, CAS. Glycerol (Molecular formula: $HOCH_2CHOHCH_2OH$; CAS number: 56-81-5; M_W: 92.09 g mol^{-1}; purity: ≥98%) was bought from Beijing Solarbio Science & Technology Co., Ltd. The molecular structures of $[N_{4444}][NTf_2]$ and glycerol were shown in Scheme 1. All chemicals were used as received.

Basic characterizations

The Fourier Transform infrared (FTIR) spectrum of $[N_{4444}][NTf_2]$ powders at room temperature was recorded in the spectral range of 400–4000 cm^{-1} at a resolution of 4 cm^{-1} using an FTIR spectrometer (INVENIO-R, Bruker) with an attenuated total reflection (ATR) accessory. The NMR spectra were recorded on a Bruker Avance™ II 400 MHz spectrometer at room temperature. Powder XRD measurements of fine powders of $[N_{4444}][NTf_2]$ were performed at room temperature under vacuum on a powder X-ray diffractometer (Empyrean, PANalytical) using Cu K_α radiation (λ = 1.5406 Å) to identify the crystalline structure of $[N_{4444}][NTf_2]$. The measurement is composed of θ–2θ scan from 5 to 60° with a step size of 0.026°. The full instrumental specifications and experimental parameters are detailed in the (ESI†).

Differential scanning calorimetry (DSC) measurements

DSC measurements were conducted between −150 °C and 335 °C on a DSC3 STARe system (METTLER TOLEDO) at a heating/cooling rate of 10 °C min^{-1} to identify the melting point (T_m) of $[N_{4444}][NTf_2]$ and the liquid temperature range. Additionally, the three-step measurements (isothermal → ramp → isothermal) were carried out over the temperature ranges of −100 to −50, −10 to 25 °C and 95 to 195 °C to determine the heat capacities of the solid and liquid states of $[N_{4444}][NTf_2]$. The experimental results of heat capacities are shown in the ESI.†

Thermogravimetric analysis (TGA)

The thermal properties of $[N_{4444}][NTf_2]$ and glycerol were recorded on a thermogravimetric analyzer Q5000 (TA Instruments) using the same platinum crucible (volume: 78.5 mL; cross-sectional area (a): 0.785 cm^2). Isothermogravimetric analysis (IGA) experiments of $[N_{4444}][NTf_2]$ were conducted under a nitrogen atmosphere (60 mL min^{-1}) at 230, 260, 290, 310, 330 and

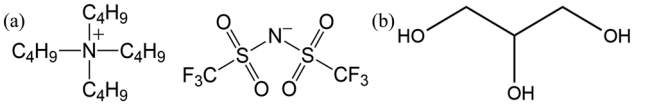

Scheme 1 The chemical structures of $[N_{4444}][NTf_2]$ (a) and glycerol (b).

350 °C successively for 1 h, respectively. Before the IGA measurement, the sample was heated from room temperature to 250 °C at a heating rate of 20 °C min^{-1} and was held at that temperature for one hour so as to remove possible volatile impurities and water and completely spread the melts in the pan. Afterwards, it was heated or cooled to the target temperatures. The experiments on glycerol were conducted under the same nitrogen atmosphere (60 mL min^{-1}) at 100, 120, 140, and 160 °C for 20 min, respectively. The initial mass of each sample was measured to be between 50.104 and 52.167 mg. Concerning the ramped TGA measurements of $[N_{4444}][NTf_2]$, it was guaranteed that each sample possessed an initial mass of around 18 mg and was heated from room temperature to 750 °C at heating rates of 5, 10, and 15 °C min^{-1}, respectively, in a nitrogen atmosphere (60 mL min^{-1}).

Density functional theory (DFT) calculations

Density functional theory (DFT) calculations were performed to generate the electrostatic potential maps of the cations and anions through the Dmol^3 module in Materials studio software (version 8.0). The structures of ions were optimized to the local minimum, and subsequently, the electrostatic potential maps were generated from the optimized configurations. The BLYP functional was employed with generalized gradient approximation (GGA), and the basis set DNP 4.4 was utilized in the calculation.

Theoretical basis

Concept of the thermodynamic cycle of cohesive properties

Under normal experimental conditions, the vapor of aprotic ILs is validated to be ideal gas composed of isolated ion pairs.[13] Thus, the cohesive energy (E_{coh}) of ILs is the energy required to separate the ions in a condensed state into independent ion pairs.[15] E_{coh} corresponds to the change in internal energy (ΔU_{vap} or ΔU_{sub}) during the transition from condensed matter to the vapor phase, it has relations with ΔH_{vap} or ΔH_{sub} of ILs (eqn (1) and (2)). For liquid state ($PV = RT$, molar quantities):

$$E_{coh} = \Delta U_{vap} = \Delta H_{vap} - RT \quad (1)$$

for solid state:

$$E_{coh} = \Delta U_{sub} = \Delta H_{sub} - RT \quad (2)$$

where R denotes the universal gas constant (8.314 J K^{-1} mol^{-1}), and T represents the absolute temperature (K).

In the first Born–Fajans–Haber (Fig. 1(a)), the ΔH_{sub} is regarded as the summation of ΔH_{vap}, fusion enthalpy (ΔH_{fus}) and the enthalpy of a solid–solid phase transition ($\Delta H_{CrII \rightarrow CrI}$). Moreover, the changes in ΔH_{sub} and ΔH_{vap} induced by the variation of temperature are offset by Kirchhoff's law. Thus, the relation between the parameters is described as:

$$\Delta H_{vap}(T) = \Delta H_{vap}(T_a) + \int_{T_a}^{T} \Delta_l^g C_p(T) dT \quad (3)$$

where the integration term is the contributions of Kirchhoff's law, $\Delta_l^g C_p$ indicates the difference in molar heat capacities between the gaseous ($C_{p,g}$) and the liquid state ($C_{p,l}$), and T_a signifies the average value of the experimental temperature range in the measurements of ΔH_{vap}. As reflected in eqn (3), ΔH_{vap} at melting temperature (T_m) can be calculated when $T = T_m$, marked as $\Delta H_{vap}(T_m)$. The given $\Delta H_{vap}(T_m)$ combined with ΔH_{fus} and $\Delta H_{CrII \rightarrow CrI}$ equal the sublimation enthalpy at a melting point ($\Delta H_{sub}(T_m)$). Moreover, the additional contributions of Kirchhoff's law in the temperature range of solid state

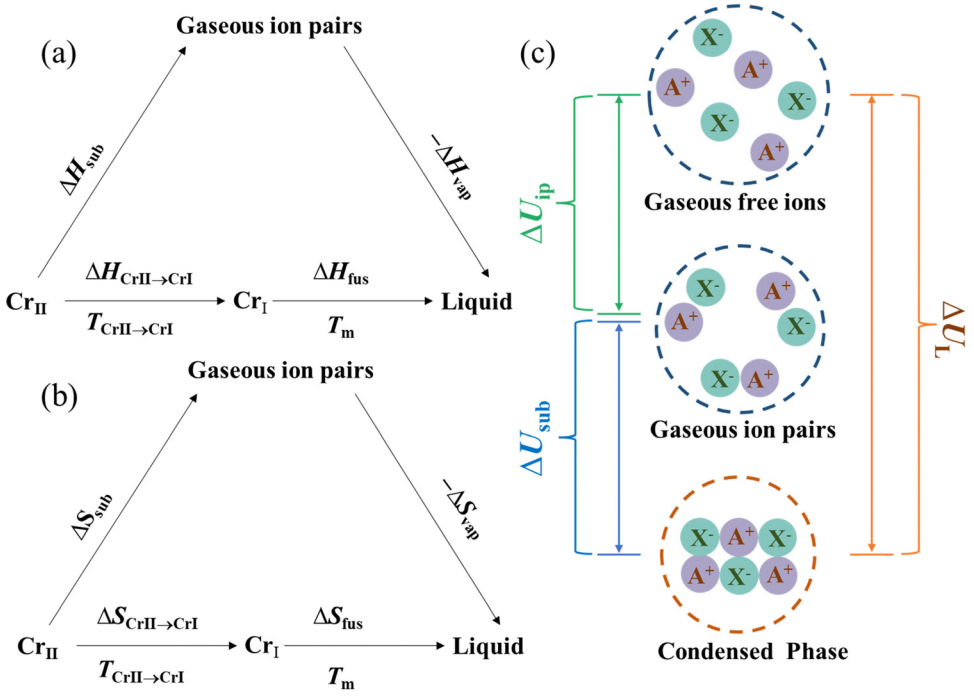

Fig. 1 The Born–Fajans–Haber cycles of enthalpy (a), entropy (b) and internal energy (c).

should also be included in eqn (4):

$$\Delta H_{sub}(T) = \Delta H_{vap}(T_m) + \Delta H_{fus} + \int_{T_m}^{T} \Delta_s^g C_p(T)\mathrm{d}T \quad (4)$$

where the integration term is the contribution of Kirchhoff's law in the temperature range of solid state, and $\Delta_s^g C_p$ represents the difference in molar heat capacities between the gaseous ($C_{p,g}$) and the solid state ($C_{p,s}$). If the temperature of interest is lower than the solid–solid transition temperature ($T_{CrII \rightarrow CrI}$), $\Delta H_{CrII \rightarrow CrI}$ should be added into the cycle of phase transition enthalpy (eqn (5)).

$$\Delta H_{sub}(T) = \Delta H_{sub}(T_m) + \Delta H_{CrII \rightarrow CrI} + \int_{T_m}^{T} \Delta_s^g C_p(T)\mathrm{d}T \quad (5)$$

$\Delta S_{vap}(T_a)$ is calculated from $\Delta S_{vap}(T_b)$ using $\Delta_l^g C_p(T_a)$, where T_b denotes the theoretical boiling point of $[N_{4444}][NTf_2]$, and $\Delta S_{vap}(T_b)$ equals $\Delta H_{vap}/T_b$ (eqn (6)). T_b can be extrapolated from the Antoine equation of $[N_{4444}][NTf_2]$ when the vapor pressure (P_{vap}) equals the standard pressure (10^5 Pa).

$$\Delta S_{vap}(T_a) = \Delta S_{vap}(T_b) + \Delta_l^g C_P(T_a) \ln\left(\frac{T_a}{T_b}\right) \quad (6)$$

$$\lg P_{vap} = A - C/(T + C) \quad (7)$$

Specifically, ΔS_{vap} and ΔS_{sub} are derived from $\Delta S_{vap}(T_b)$ based on the Born–Fajans–Haber cycle (Fig. 1(b)) and additional integration term representing the contribution of Kirchhoff's law:

$$\Delta S_{vap}(T) = \Delta S_{vap}(T_a) + \int_{T_a}^{T} \Delta_l^g C_P(T)\frac{1}{T}\mathrm{d}T \quad (8)$$

Similarly, $\Delta S_{vap}(T_m)$ can be calculated when $T = T_m$. Regarding the calculated ΔS_{sub} in the temperature range of solid state, the entropy of solid–solid transition ($\Delta S_{CrII \rightarrow CrI}$) between the melting point and objective temperature, apart from the fusion entropy (ΔS_{fus}), should be added into the equation (eqn (9)).

$$\Delta S_{sub}(T) = \Delta S_{sub}(T_m) + \Delta S_{fus} + \Delta S_{CrII \rightarrow CrI} + \int_{T_m}^{T} \Delta_s^g C_P(T)\frac{1}{T}\mathrm{d}T \quad (9)$$

The lattice potential energy (U_L) of crystalline ionic liquids can be approximated to its electrostatic interaction potential energy (E_{es}). Then, E_{es} can be calculated by multiplying the Madelung constant with the electrostatic interaction energy of single ion pair in the crystal (eqn (10)).

$$E_{es} = -\frac{M|Z_+||Z_-|e^2}{4\pi\varepsilon_0 r_{min}} \quad (10)$$

where Z_+ and Z_- denote the charge of the cation and anion, respectively; e represents the element charge (1.602×10^{-19} C); ε_0 stands for the vacuum permittivity (8.854×10^{-12} F m^{-1}); M refers to Madelung constant. The calculation of the Madelung constant adopts the expanding unit-cell generalized numerical (EUGEN) method[16] (ESI†). The formula for lattice potential energy implies that the value of the internal energy corresponding to the gas phase free ions is taken as the zero potential energy point, thus the change in internal energy occurring during the conversion from a crystal to the gaseous free ions, lattice energy (ΔU_L), equals the negative lattice potential energy ($-U_L$): $\Delta U_L = -U_L$. Similarly, the change of internal energy corresponding to the conversion from the ion pairs to the free ions of gas phase, internal energy of gaseous ion pairs (ΔU_{ip}), is equal to the negative potential energy of ion pairs ($-U_{ip}$): $\Delta U_{ip} = -U_{ip}$. The relations between ΔU_L, ΔU_{sub} and internal energy of gaseous ion pairs (ΔU_{ip}) are presented in Fig. 1(c) and eqn (11).

$$\Delta U_{sub} = \Delta U_L - \Delta U_{ip} \quad (11)$$

The approximation of U_{ip} given by the Born–Mayer equation[17] is:

$$U_{ip} = -\frac{|Z_+||Z_-|e^2 N_A}{4\pi\varepsilon_0 r_{12}} 10^6 \left(1 - \frac{\rho_0}{r_{12}}\right) \quad (12)$$

where N_A is Avogadro constant (6.022×10^{23}), ρ_0 represents a constant usually taken as 0.0345 nm, and r_{12} denotes the separated distance of the positive and negative charge in the single ion pair of gas phase. Thus, ΔU_{ip} and r_{12} can be estimated using the known ΔU_L and E_{coh}.

The detailed calculation methods of ΔH_{vap}, P_{vap} and ΔU_L were discussed in the ESI.†

Pyrolysis kinetic method

The pyrolysis kinetic parameters were analyzed by differential and integral methods (ESI†). The differential ones contain Ozawa, Kissinger, and Starink methods, which derive the activation energy (E_a), pre-exponent factor (A), kinetic exponent (n), enthalpy change (ΔH), entropy change (ΔS), and Gibbs free energy change (ΔG) during the formation of transition state through the DTG data from TGA experiments. Meanwhile, the integral ones consist of Flynn–Wall–Ozawa (ASTM E-1641), Kissinger–Akahira–Sunose (KAS), and Starink methods. The E_a at different degradation conversions (α) was calculated using the integral methods.

Results and discussions

Cohesive properties

ΔH_{vap} as an essential part of the Born–Fajans–Haber cycle is the first cohesive property to be determined. Hence, the ΔH_{vap} of $[N_{4444}][NTf_2]$ was measured using the IGA method at its experimental average temperature (T_a = 295 °C) (ESI†). Except for ΔH_{vap}, the other components of the cycle are the enthalpies of phase change in the condensed state. As expected, $[N_{4444}][NTf_2]$ has only a micro solid–solid phase change at −29.4 °C, where the two solid phases were denoted as phases Cr_I and Cr_{II} corresponding to the phase at a higher and lower temperature, respectively (Fig. 2). In the XRD pattern, a similar phenomenon was observed (Fig. S3, ESI†). Moreover, the discontinuous change of heat capacities of $[N_{4444}][NTf_2]$ (Fig. 3(a)) can also demonstrate the occurring of phase change at −29.4 °C. The known $\Delta H_{vap}(T_a)$, ΔH_{fus} and $\Delta H_{CrII \rightarrow CrI}$ are 144.2, 23.3 and 0.88 kJ mol^{-1}, respectively, forming the Born–Fajans–Haber cycle of enthalpy to derive ΔH_{sub}. The used $\Delta H_{vap}(T_a)$, ΔH_{fus}, T_a

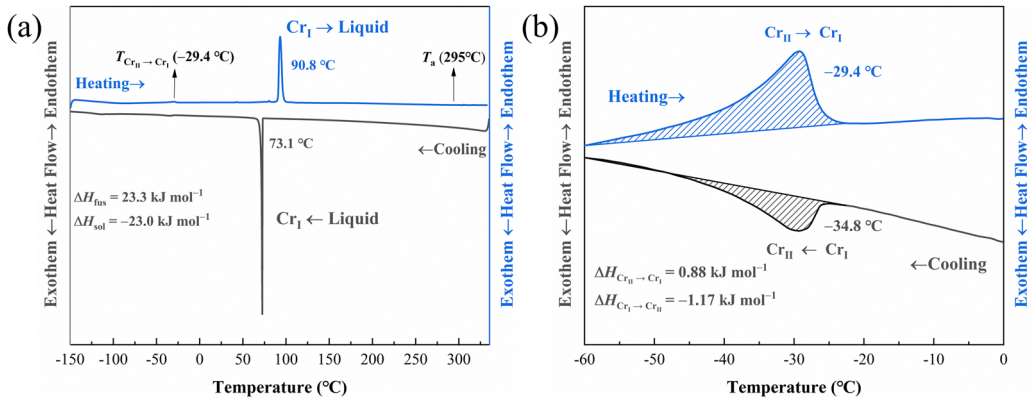

Fig. 2 DSC thermogram of $[N_{4444}][NTf_2]$ measured at 10 °C min^{-1} for both the heating and cooling process at −150 °C to 335 °C (a), and its enlarged view at −60 °C to 0 °C (b).

and T_m of $[N_{4444}][NTf_2]$, $[C_2mim][NTf_2]$[18,19] and $[C_4mim][NTf_2]$[20,21] are listed in Table 1. However, the calculation of ΔH_{sub} from the thermodynamic cycle involves two parts, which correspond to the phase change (the above-mentioned results) and the temperature variation, respectively. The dependence of molar heat capacities of Cr_I and Cr_{II} ($C_{p,s}$), liquid ($C_{p,l}$), and gas phase ($C_{p,g}$) on the temperature is fitted using polynomial regression to demonstrate the changes in ΔH_{vap} and ΔH_{sub} caused by the temperature variation (Fig. 3(a)). The parameters of polynomials and correlation factor R^2 for $[N_{4444}][NTf_2]$ were listed in Table 2. Notably, the selected ranges for fitting are the parts of experimental $C_{p,s}$ and $C_{p,l}$, since these experimental results are associated with the temperature far from the phase change point and then reinforce the accuracy of heat capacities. For the ideal gas phase of $[N_{4444}][NTf_2]$, $C_{p,g}$ was assumed as the sum of the contribution of cation and anion.[22] The detailed calculations for the molar heat capacities of $[N_{4444}]^+$ and $[NTf_2]^-$ were presented in ESI.† Additionally, the parameters of the polynomials for $C_{p,s}$, $C_{p,l}$ and $C_{p,g}$ of $[C_2mim][NTf_2]$ and $[C_4mim][NTf_2]$ were listed in Tables S4 and S5 (ESI†). As derived by Kirchhoff's law (eqn (4)), the change in ΔH_{vap} and ΔH_{sub} of $[N_{4444}][NTf_2]$ exhibit an increasing tendency with decreasing temperature (Fig. 3(b)).

Therefore, the sum of $\Delta H_{vap}(T_a)$, ΔH_{fus}, $\Delta H_{CrII \rightarrow CrI}$ and the change in enthalpy enables the accurate value of ΔH_{vap} or ΔH_{sub} and E_{coh} at a given temperature (Fig. 4, 5 and Tables S8–S10, ESI†). It has a negative correlation between E_{coh} and temperature in the total liquid temperature range of all the three ILs. As the temperature decreases from 295 to 90.8 °C, E_{coh} of

Table 1 The used $\Delta H_{vap}(T_a)$, ΔH_{fus}, T_a and T_m of selected ILs

IL	ΔH_{vap} (T_a) (kJ mol^{-1})	T_a (°C)	ΔH_{fus} (kJ mol^{-1})	T_m (°C)	Ref.
$[N_{4444}][NTf_2]$	144.2	295.0	23.3	−29.8	This work
$[C_2mim][NTf_2]$	122	124.4	21.9	−1.7	18,19
$[C_4mim][NTf_2]$	118.3	204.5	19.9	6.9	20,21

Table 2 The parameters of polynomials for heat capacities of solid ($C_{p,s}$), liquid ($C_{p,l}$) and gas ($C_{p,g}$) phases of $[N_{4444}][NTf_2]$ on temperatures

Parameters	$C_{p,s}$		$C_{p,l}$	$C_{p,g}$
	Cr_{II}	Cr_I		
a_0	−53.13	260.02	−168.23	10.21
a_1	2.68	0.66	4.57	2.31
a_2	-1.34×10^{-3}	2.76×10^{-3}	-3.97×10^{-3}	-1.19×10^{-3}
a_3	—	—	—	4.16×10^{-7}
R^2	0.999	0.999	0.999	0.999

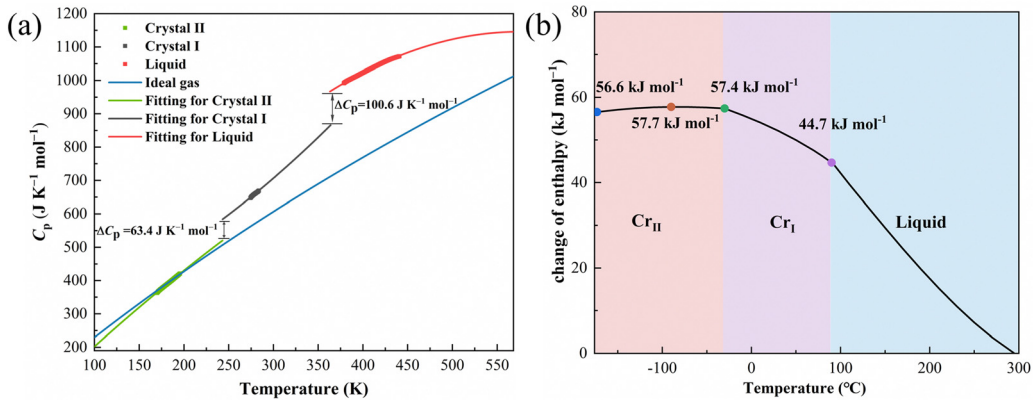

Fig. 3 Heat capacities of Cr_{II}, Cr_I, liquid and ideal gas states of $[N_{4444}][NTf_2]$ (a); Change in enthalpy due to the temperature variation (b).

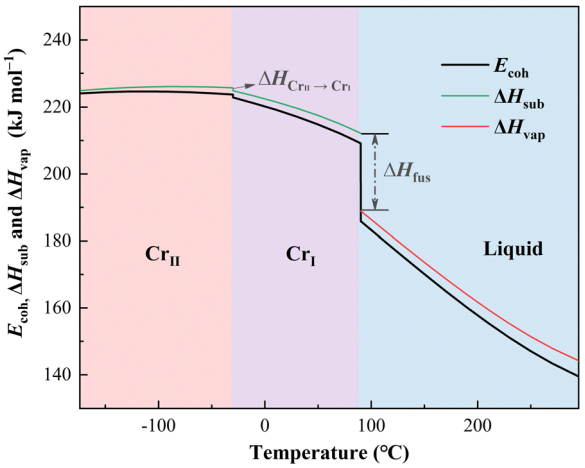

Fig. 4 The cohesive energy (E_{coh}), enthalpy of vaporization (ΔH_{vap}) and sublimation (ΔH_{sub}) of [N_{4444}][NTf_2] from −173.15 to 295 °C.

[N_{4444}][NTf_2] varies from 139.5 to 185.8 kJ mol^{-1} (Fig. 4), while E_{coh} of [C_2mim][NTf_2] ranges from 118.7 to 137.4 kJ mol^{-1} in [124.4 °C, −1.7 °C] and E_{coh} of [C_4mim][NTf_2] ranges from 114.3 to 144.8 kJ mol^{-1} in [204.5 °C, 6.9 °C] (Fig. 5). During the solid-state temperature range, nonetheless, the E_{coh} *versus* temperature of the three solid organic salts have diverse tendencies. For the solid phase of [N_{4444}][NTf_2], the E_{coh} at a temperature slightly lower than 90.8 °C is 209.1 kJ mol^{-1}. E_{coh} of solid-state [N_{4444}][NTf_2] has monotonical negative correlation with temperature in the total Cr_I phase and higher-temperature region of the Cr_{II} phase range, whereas it reaches its maximum value of 224.7 kJ mol^{-1} at −110 °C. This can be attributed to that $C_{p,s}$ is slightly lower than $C_{p,g}$ below −110 °C for [N_{4444}][NTf_2]. As the temperature decreases, the E_{coh} of [N_{4444}][NTf_2] reaches to 224.1 kJ mol^{-1} at −173.15 °C. In contrast, E_{coh} of solid-state [C_2mim][NTf_2] and [C_4mim][NTf_2] show negative correlations with temperature in the total solid temperature (Fig. 5). For [C_2mim][NTf_2] and [C_4mim][NTf_2] solid organic salts, the E_{coh} at −153.15 °C are 165.4 and 169.6 kJ mol^{-1}, respectively. Moreover, the calculated E_{coh} of [C_2mim][NTf_2] at −273.15 °C is 166.8 kJ mol^{-1}, while the reported values of E_{coh} of [C_2mim][NTf_2] calculated by different quantum chemical methods range from 161.7 to 171.2 kJ mol^{-1} at −273.15 °C,[11] with a deviation lower than 3% from the value in this work, demonstrating the reliability of the method used in this paper. For the three organic salts, the abrupt increase in E_{coh} corresponds to a first-order phase change (*i.e.* solidification). This suggests that the new phase is more stable than the old one in thermodynamics when the temperature is lower than the transition point.

Additionally, a theoretical boiling point (T_b) of ILs can be defined as the temperature at which the Gibbs energy of vaporization (ΔG_{vap}) equals zero. Therefore, ΔH_{vap} at T_b can be used to calculate the entropy of vaporization (ΔS_{vap}) and sublimation (ΔS_{sub}). T_b of ILs does not exist in the actual conditions because the thermal decomposition would occur prior to the boiling. Nonetheless, the theoretical T_b can be regarded as the extrapolated value of temperature at which P_{vap} equals the standard pressure (10^5 Pa) in the function of P_{vap} about temperature. Besides, the P_{vap} of [N_{4444}][NTf_2] is calculated using the IGA experiments data (Table S11, ESI†) to obtain T_b and $\Delta H_{vap}(T_b)$ of [N_{4444}][NTf_2], and it ranges from 0.02 to 14.3 Pa between 230 and 350 °C. The data of P_{vap} at literatures[23,24] are adopted for the calculations of ILs [C_4mim][NTf_2] and [C_2mim][NTf_2]. Moreover, the function of P_{vap} is described with the Antoine equation (ESI†). Subsequently, T_b of [N_{4444}][NTf_2], [C_4mim][NTf_2], and [C_2mim][NTf_2] is determined to be 587.5, 393.6 and 842.1 °C, respectively. However, $\Delta_l^g C_p$ between T_b and T_a do not conform to a polynomial function. Thus, $\Delta_l^g C_p(T_a)$ was utilized as a rough approximation of the $\Delta_l^g C_p$ to calculate $\Delta H_{vap}(T_b)$. The determined values of $\Delta H_{vap}(T_b)$ and $\Delta S_{vap}(T_b)$ of [N_{4444}][NTf_2] amount to 105.3 kJ mol^{-1} and 122.4 J K^{-1} mol^{-1}, respectively. As the intersections of the cycle, ΔS_{fus} and $\Delta S_{CrII \rightarrow CrI}$ have values of 64.1 and 3.6 J K^{-1} mol^{-1}, respectively, derived from ΔH_{fus} and $\Delta H_{CrII \rightarrow CrI}$. Then, ΔS_{vap} and ΔS_{sub} of [N_{4444}][NTf_2] were extrapolated to a given temperature (Fig. 6(a)) by the Born–Fajans–Haber cycle of entropy. Similarly, ΔS_{vap} and ΔS_{sub} of [C_4mim][NTf_2] and [C_2mim][NTf_2] were also calculated by this approach. The results are employed to calculate ΔG_{vap} and the Gibbs free energy of sublimation (ΔG_{sub}). The detailed results of the three organic salts were

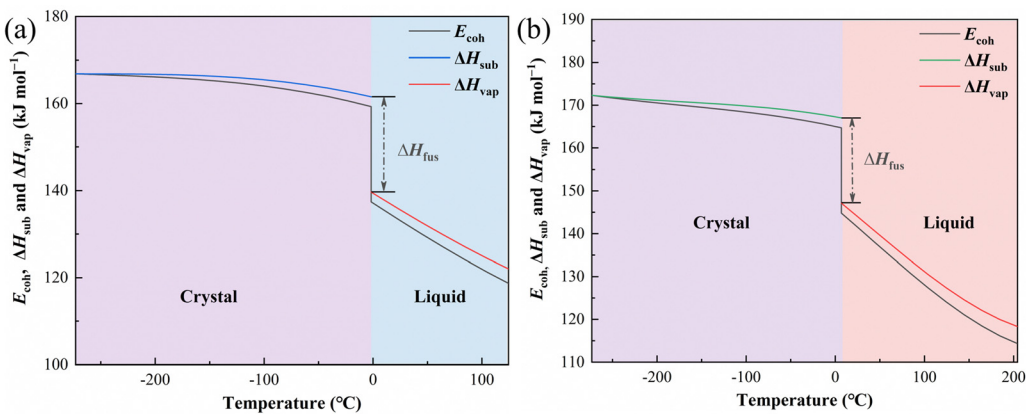

Fig. 5 The cohesive energy (E_{coh}), enthalpy of vaporization (ΔH_{vap}), and sublimation (ΔH_{sub}) of [C_2mim][NTf_2] from −273.15 to 124.35 °C (a) and [C_4mim][NTf_2] from −273.15 to 204.45 °C, respectively.

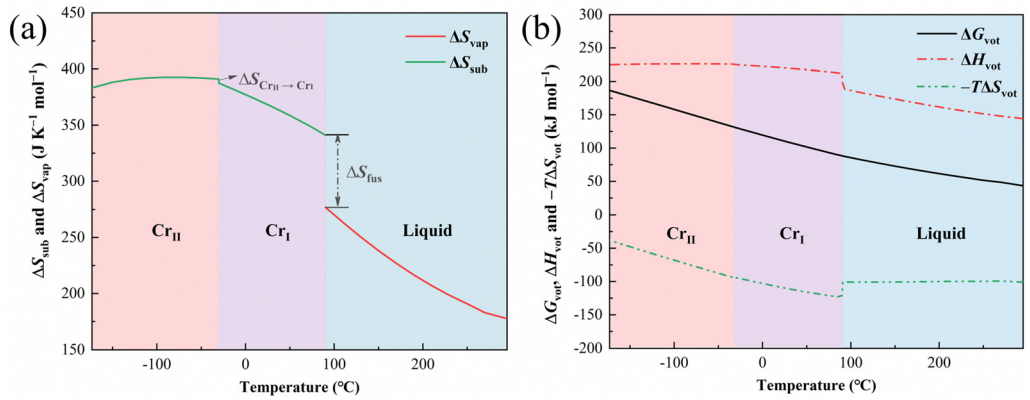

Fig. 6 The entropy of vaporization (ΔS_{vap}) and sublimation (ΔS_{sub}) of $[N_{4444}][NTf_2]$ from −173.15 to 295 °C (a); the enthalpy of vaporization or sublimation (ΔH_{vot}), the $-T$ (K) × entropy of vaporization or sublimation ($-T\Delta S_{vot}$) and Gibbs free energy of vaporization or sublimation (ΔG_{vot}) of $[N_{4444}][NTf_2]$ from −173.15 to 295 °C (b).

listed in Tables S12–S17 (ESI†), respectively. With the purpose of simplifying the marks of the cohesive properties, the terms of ΔH_{sub} and ΔH_{vap} were unified as ΔH_{vot}, ΔS_{sub} and ΔS_{vap} as ΔS_{vot}, and ΔG_{vap} and ΔG_{sub} as ΔG_{vot} in Fig. 6 and 7. The results demonstrate that the phase change in the condensed state of ILs has a negligible effect on ΔG_{vot} and a significant one on ΔH_{vot} and ΔS_{vot}. ΔG_{vot} of $[N_{4444}][NTf_2]$ ranges from 43.3 to 186.6 kJ mol^{-1} in [295 °C, −173.15 °C], and ΔG_{vot} of $[C_4mim][NTf_2]$ ranges from 29.3 to 164.2 kJ mol^{-1} in [204.45 °C, −252.85 °C], however, that of $[C_2mim][NTf_2]$ varies from 60.6 to 166.4 kJ mol^{-1} in [124.4 °C, −271.7 °C]. Thus, the average rate of ΔG_{vot} variation with temperature of $[C_2mim][NTf_2]$ is lower than the former tow organic salts. In other words, ΔG_{vot} of $[N_{4444}][NTf_2]$ and $[C_4mim][NTf_2]$ has higher temperature sensitivity than that of $[C_2mim][NTf_2]$. This difference may be ascribed to the longer alkyl chains in the cations of the former two salts since more carbon and hydrogen atoms can induce a larger absolute value of $\Delta_l^g C_p$ and $\Delta_s^g C_p$.[25]

Fig. 1(c) depicts the third cycle, which is closed by the ΔU_{sub}, the lattice energy (ΔU_L) and the internal energy of gaseous ion pairs (ΔU_{ip}). Fig. 8(a) and (b) demonstrate the asymmetric cell and equilibrium geometries of $[N_{4444}][NTf_2]$ at 173.15 °C. $[N_{4444}][NTf_2]$ is monoclinic with a dipole moment of the unit cell of 29.53 Debye. The electrostatic potential maps (Fig. 8(c) and (d)) imply that the positive charge in cation is concentrated on the nitrogen atom rather than the hydrogen atom, and there are generally no H-bonds regarding C–H. Thus, no possible H-bonds site exits in $[N_{4444}]^+$ and $[NTf_2]^-$. Furthermore, the contributions of van der Waals interaction on the U_L for simple ionic solids are only about 1%[26] revealing that the U_L of $[N_{4444}][NTf_2]$ approximately equals its pure electrostatic interaction energy in this case (E_{es}). Similarly, the U_L of the other two ILs can be determined based on this approximation. With the crystal structure data of $[N_{4444}][NTf_2]$ at −173.15 °C[27] and $[C_2mim][NTf_2]$ and $[C_4mim][NTf_2]$ at −153.15 °C,[28] the ΔU_L together with the M and r_{min} (ESI†) are determined using the EUGEN method. The ΔU_L and ΔU_{sub} of $[N_{4444}][NTf_2]$ at −173.15 °C are 408.3 and 224.1 kJ mol^{-1}, respectively, while the M of $[N_{4444}][NTf_2]$ is 1.205 and r_{min} is 0.410 nm. Thus, the difference between ΔU_L and ΔU_{sub} unveils that ΔU_{ip} equals 184.2 kJ mol^{-1}. The detailed results of the other two solid organic salts at −153.15 °C were provided in Table 3. The given ΔU_{ip} can estimate r_{12} of $[N_{4444}][NTf_2]$, $[C_2mim][NTf_2]$ and $[C_4mim][NTf_2]$ through the Born–Mayer equation (eqn (12)). Meanwhile, r_{12} is much larger than r_{min} for the three organic salts, indicating that the charge separation in the ion pair is

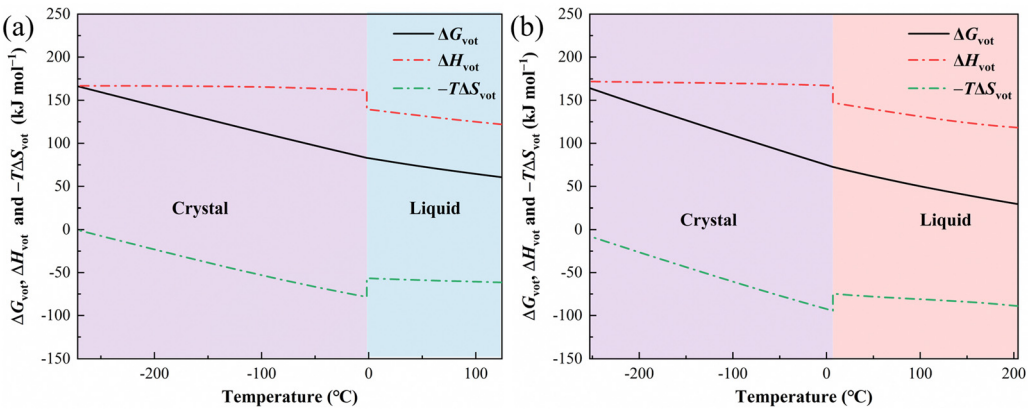

Fig. 7 The enthalpy of vaporization or sublimation (ΔH_{vot}), the $-T$ (K) × entropy of vaporization or sublimation ($-T\Delta S_{vot}$) and Gibbs free energy of vaporization or sublimation (ΔG_{coh}) of $[C_2mim][NTf_2]$ from −271.71 to 124.35 °C (a) and $[C_4mim][NTf_2]$ from −252.85 to 204.45 °C (b), respectively.

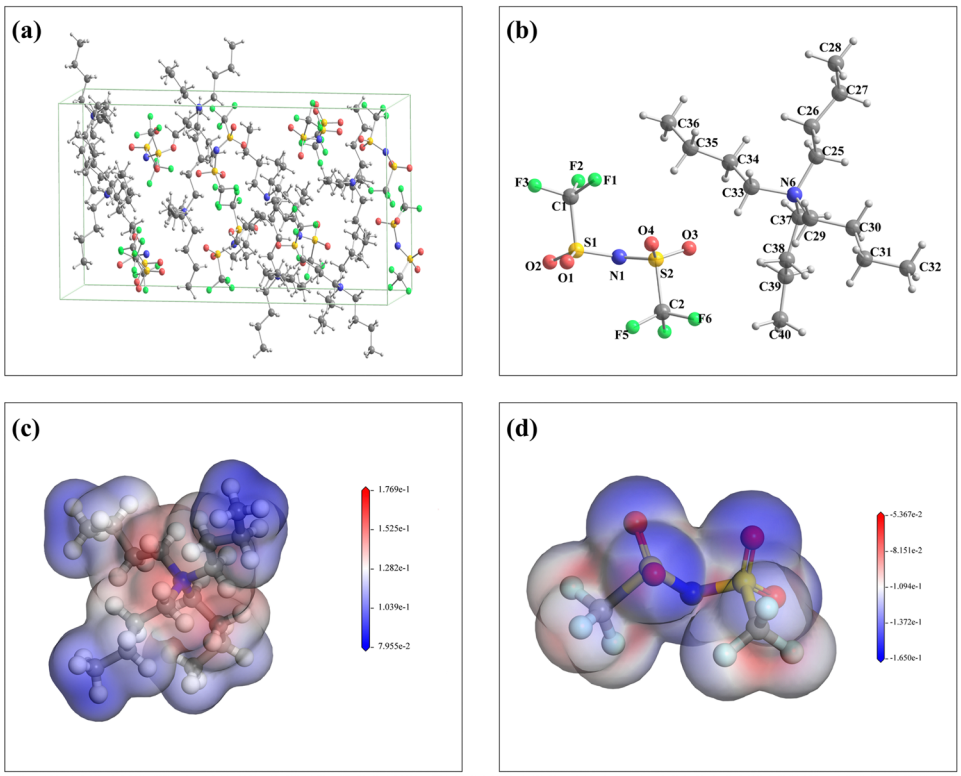

Fig. 8 Illustration of the asymmetric cell (a) and equilibrium geometries of ions (b) for the $[N_{4444}][NTf_2]$ at −173.15 °C. Representation of the electrostatic potential on an isosurface of electronic density (isovalue = 0.017) for $[N_{4444}]^+$ (c) and $[NTf_2]^-$ (d); negative areas shaded in blue and the positive in red.

stronger than the closet counterion in the solid phase for aprotic ILs. The ratios "r_{12}/r_{min}" of $[N_{4444}][NTf_2]$, $[C_4mim][NTf_2]$, and $[C_2mim][NTf_2]$ are 1.75, 1.18 and 1.10, respectively. It reflects that r_{12}/r_{min} may increase with the growing numbers of carbon atoms in alkyl chains since more adjacent but unbonded atoms can result in a larger van der Waals radius in the gas phase. This explanation requires further investigation.

Pyrolysis mechanism

The onset temperature (T_{onset}) of thermal decomposition is determined using the ramped TGA technique to access the thermal stability of $[N_{4444}][NTf_2]$ (Table S18, ESI†). The pyrolysis kinetics of $[N_{4444}][NTf_2]$ are analyzed using the Ozawa, Kissinger, and Starink methods from the differential thermal gravimetric (DTG) peak temperatures (Table 4). T_{onset} presents an extremely high linear relation with heating rates, where the correlation R^2 exceeds 0.9999. Thus, the heating rate is extrapolated to 0 °C min^{-1}, and the T_{onset} is obtained as 368.5 °C at that rate. As derived through Ozawa, Kissinger and Starink methods, the average activation energy (E_a) is 242.1 kJ mol^{-1}, highlighting the exceptional thermal stability of $[N_{4444}][NTf_2]$. Moreover, the enthalpy (ΔH) and entropy (ΔS) change during the formation of the transition state are 237.4 kJ mol^{-1} and 57.1 J K^{-1} mol^{-1}, respectively. ΔS is minimal compared with ΔH. Therefore, it can be postulated that the transition state of $[N_{4444}][NTf_2]$ is far from its initial state, leading to low reactivity. The calculation of the kinetic exponent (n = 0.005) reflects that the pyrolysis of $[N_{4444}][NTf_2]$ is a zero-order reaction (ESI†). The half-life ($t_{1/2}$) of $[N_{4444}][NTf_2]$ is derived from the kinetic parameters (Table S19, ESI†).

Table 3 The calculated features of $[N_{4444}][NTf_2]$, $[C_2mim][NTf_2]$ and $[C_4mim][NTf_2]$

Features	$[N_{4444}][NTf_2]$	$[C_2mim][NTf_2]$	$[C_4mim][NTf_2]$
ΔU_L (kJ mol^{-1})	408.3	452.0	439.6
ΔU_{sub} (kJ mol^{-1})	224.1	165.4	140.8
ΔU_{ip} (kJ mol^{-1})	184.2	286.6	311.2
M	1.205	1.329	1.277
r_{min} (nm)	0.410	0.408	0.403
r_{12} (nm)	0.718	0.447	0.477
T (°C)	−173.15	−153.15	−153.15

In the kinetics analysis at different degradation conversions (α), Flynn–Wall–Ozawa (ASTM E-1641), Kissinger–Akahira–Sunose (KAS), and Starink methods are employed to derive the E_a at the conversion of 5 to 90%. The results demonstrate that E_a of $[N_{4444}][NTf_2]$ has reduced dependence with the increasing degradation conversion and becomes a constant value at the conversion of 70% (Fig. 9). The variations of E_a are attributed to the increased temperature during the thermal gravimetric experiments since this degradation process is a zero-order reaction. Thus, the pyrolysis process of $[N_{4444}][NTf_2]$ is a multi-step process consisting of an endothermic reversible reaction followed by an irreversible one.[29] E_a is the sum of the activation enthalpy of the reversible reaction (ΔH^0) and the activation energy of the irreversible reaction (E_2) (ESI†). The endothermic reversible reaction's equilibrium constant (K_1)

Table 4 Pyrolysis kinetic parameters of $[N_{4444}][NTf_2]$ using Ozawa, Kissinger, and Starink methods through DTG peak temperatures

Method	E_a (kJ mol^{-1})	ln A (min^{-1})	R^2	ΔH (kJ mol^{-1})	ΔG (kJ mol^{-1})	ΔS (J K^{-1} mol^{-1})
Ozawa	244.3	42.4	0.998	238.6	198.6	58.0
Kissinger	241.9	42.0	0.999	236.2	198.6	54.9
Starink	244.0	42.4	0.998	238.3	198.6	58.4
Avarage	242.1	42.3		237.7	198.6	57.1

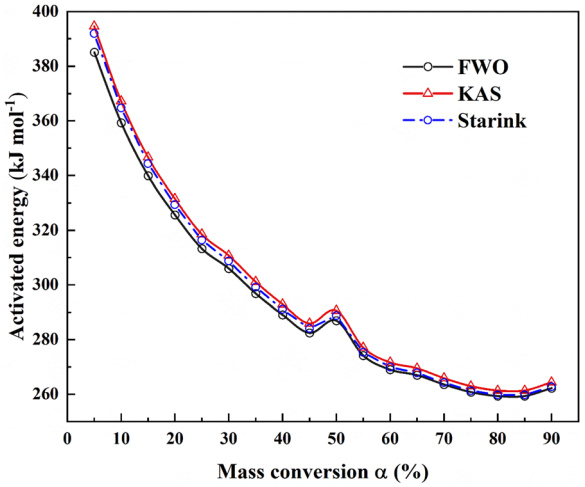

Fig. 9 Activation energy (E_a) of a $[N_{4444}][NTf_2]$ at different degrees of conversion.

increases with the increasing temperature, reducing the value of ΔH^0. ΔH^0 tends to be zero when the condition of $K_1 \gg 1$ is fulfilled at a high temperature. Hence, the minimum value of E_a approximately equals the activation energy of the irreversible reaction (259.3 kJ mol^{-1}), revealing that the irreversible reaction is a rate-determining step (RDS) in the pyrolysis process of $[N_{4444}][NTf_2]$. Furthermore, the discussions and data associated with cohesive properties and pyrolysis kinetics are available in the ESI.†

Conclusions

In this paper, three Born–Fajans–Haber cycles were adopted to describe the cohesive properties of the condensed state of $[N_{4444}][NTf_2]$, $[C_2mim][NTf_2]$, and $[C_4mim][NTf_2]$, providing a novel method to detect the cohesive properties of ILs. The internal energy (or cohesive energy), enthalpy, entropy, and Gibbs free energy of the transition from condensed state to gas were successfully derived from the method. Moreover, the internal energy of the gas phase and the charge separation of the single gaseous ion pair were estimated from the cycle. Concerning thermal degradation, $[N_{4444}][NTf_2]$ has extremely high thermal stability. The characteristics of condensed matter of the three ILs can be summarized as follows:

(1) Longer alkyl chains in cations resulted in higher temperature sensitivity of Gibbs free energy change during the transition from the condensed matter to vapor for aprotic ILs.

(2) The degree of charge separation in the gaseous ion pair was larger than that of the ions in the solid phase.

(3) A longer alkyl chain in cation enlarged the charge separation distance in ion pair and the ratio r_{12}/r_{min} of aprotic ILs.

(4) The pyrolysis process of $[N_{4444}][NTf_2]$ was a multi-step process consisting of an endothermic reversible reaction followed by an irreversible one, where the irreversible one was a rate-determining step.

With the promotion of this method to more types of ILs, these thermodynamic cycle concepts would enlighten research on the nature of the gaseous state of ILs.

Abbreviation

T	Temperature (K)
t	Time (min)
m	Weight (mg)
a	Cross-sectional area of the crucible (cm^2)
M_W	Molecular weight (g mol^{-1})
N_A	Avogadro constant (6.022×10^{23})
R	Gas constant (8.314 J K^{-1} mol^{-1})
ε_0	Vacuum permittivity (8.854×10^{-12} F m^{-1})
e	Elementary charge (1.602×10^{-19} C)
M	Madelung constant
P_{vap}	Vapor pressure (Pa)
C_p	Molar heat capacity (J K^{-1} mol^{-1})
$C_{p,s}$	Molar heat capacity of solid state (J K^{-1} mol^{-1})
$C_{p,l}$	Molar heat capacity of liquid state (J K^{-1} mol^{-1})
$C_{p,g}$	Molar heat capacity of ideal gaseous state (J K^{-1} mol^{-1})
ΔH_{vap}	Enthalpy of vaporization (kJ mol^{-1})
ΔH_{sub}	Enthalpy of sublimation (kJ mol^{-1})
ΔH_{fus}	Enthalpy of fusion (kJ mol^{-1})
ΔS_{fus}	Entropy of fusion (J K^{-1} mol^{-1})
ΔH_{sol}	Enthalpy of solidification (kJ mol^{-1})
E_{coh}	Cohesive energy (kJ mol^{-1})
ΔU_{vap}	Internal energy of vaporization (kJ mol^{-1})
ΔU_{sub}	Internal energy of sublimation (kJ mol^{-1})
ΔU_L	Lattice energy (kJ mol^{-1})
ΔU_{ip}	Internal energy of ion pairs in the gaseous state (kJ mol^{-1})
r_{min}	Minimum distance between the cation and anion (nm)
r_{12}	The charge separation distance of single ion pair in the gas phase
E_a	Activation energy (kJ mol^{-1})
A	Pre-exponential factor (min^{-1})
ΔH	Enthalpy change of activated complex formation (kJ mol^{-1})
ΔG	Gibbs energy change of activated complex formation (kJ mol^{-1})
ΔS	Entropy change of activated complex formation (J K^{-1} mol^{-1})

Author contributions

Jiangshui Luo: Conceptualization, supervision, methodology, project administration, data curation, formal analysis, funding acquisition, resources, and writing – review & editing. Shijie Liu:

Investigation, formal analysis, methodology, data curation and writing – original draft. Runhong Wei: Writing – review & editing. Guangjun Ma: Writing – review & editing. Ailin Li: Investigation and writing – review & editing. Olaf Conrad: Writing – review & editing.

Conflicts of interest

J. Luo and R. Wei have filed four Chinese patent applications (ZL202210151023.7, 202210135274.6, 202210135259.1, and 202210474222.1).

Acknowledgements

This work is financially supported by Sichuan Science and Technology Program (project No.: 2022ZYD0016 and 2023JDRC0013), National Natural Science Foundation of China (project No.: 21776120), Hohhot Science and Technology Program (project No.: 2023-JieBangGuaShuai-Gao-3), and Natural Science Foundation of Fujian Province, China (project No.: 2023J01254). We appreciate the Analytical & Testing Center of Sichuan University for providing Materials Studio and we are grateful to Daichuan Ma and Daibing Luo for their help of computational simulation. Finally, we appreciate Samuel Y. S. Tan and Dr. Ekaterina I. Izgorodina (Monash University) for providing the modified version of the EUGEN code.

Notes and references

1 A. Avid, J. L. Ochoa, Y. Huang, Y. Liu, P. Atanassov and I. V. Zenyuk, *Nat. Commun.*, 2022, **13**, 6349.
2 X. Li, D. Wang, Z. He, F. Su, J. Zhang, Y. Wang, Y. Xin, H. Wang, D. Yao, M. Li and Y. Zheng, *J. Mater. Chem. A*, 2022, **10**, 13333–13344.
3 G. Li, Q. Gao, Q. Liu, C. Gui and Z. Lei, *AIChE J.*, 2023, **69**, e17914.
4 J. Luo, A. H. Jensen, N. R. Brooks, J. Sniekers, M. Knipper, D. Aili, Q. Li, B. Vanroy, M. Wübbenhorst, F. Yan, L. Van Meervelt, Z. Shao, J. Fang, Z.-H. Luo, D. E. De Vos, K. Binnemans and J. Fransaer, *Energy Environ. Sci.*, 2015, **8**, 1276–1291.
5 A. Paolella, G. Bertoni, W. Zhu, D. Campanella, A. L. Monaca, G. Girard, H. Demers, A. C. G. Nita, Z. Feng, A. Vijh, A. Guerfi, M. Trudeau, M. Armand and S. A. Krachkovskiy, *J. Am. Chem. Soc.*, 2022, **144**, 3442–3448.
6 S. L. Piper, M. Kar, D. R. MacFarlane, K. Matuszek and J. M. Pringle, *Green Chem.*, 2022, **24**, 12–117.
7 E. Fabre and S. M. S. Murshed, *J. Mater. Chem. A*, 2021, **9**, 15861–15879.
8 K. R. Seddon, M. A. Gilea, L. P. N. Rebelo, M. J. Earle, J. M. S. S. Esperança, J. A. Widegren, J. N. Canongia Lopes and J. W. Magee, *Nature*, 2006, **439**, 831–834.
9 (*a*) V. N. Emel'yanenko, S. P. Verevkin, A. Heintz, J.-A. Corfield, A. Deyko, K. R. J. Lovelock, P. Licence and R. G. Jones, *J. Phys. Chem. B*, 2008, **112**, 11734–11742; (*b*) G. A. Backer., H. Luo and S. Dai, *J. Phys. Chem. B*, 2008, **112**, 10077–10081; (*c*) C. Wang, H. Luo, H. Li and S. Dai, *Phys. Chem. Chem. Phys.*, 2010, **12**, 7246–7250; (*d*) S. P. Verevkin, D. H. Zaitsau, V. N. Emel'yanenko and A. Heintz, *J. Phys. Chem. B*, 2011, **115**, 12889–12895; (*e*) A. M. Dunaev, V. B. Motalov, L. S. Kudin and M. F. Butman, *J. Mol. Liq.*, 2016, **223**, 407–411.
10 X. Chen, H. Tang, T. Putzeys, J. Sniekers, M. Wübbenhorst, K. Binnemans, J. Fransaer, D. E. De Vos, Q. Li and J. Luo, *J. Mater. Chem. A*, 2016, **4**, 12241–12252.
11 C. Červinka, M. Klajmon and V. C. Štejfa, *J. Chem. Theory Comput.*, 2019, **15**, 5563–5578.
12 J. M. S. S. Esperança, J. N. Canongia Lopes, M. Tariq, L. M. N. B. F. Santos, J. W. Magee and L. P. N. Rebelo, *J. Chem. Eng. Data*, 2010, **55**, 3–12.
13 I. Krossing, J. M. Slattery, C. Daguenet, P. J. Dyson, A. Oleinikova and H. Weingärtner, *J. Am. Chem. Soc.*, 2007, **129**, 11296.
14 B. Wang, L. Qin, T. Mu, Z. Xue and G. Gao, *Chem. Rev.*, 2017, **117**, 7113–7131.
15 L. Glasser and D. A. Sheppard, *Inorg. Chem.*, 2016, **55**, 7103–7110.
16 E. I. Izgorodina, U. L. Bernard, P. M. Dean, J. M. Pringle and D. R. MacFarlane, *Cryst. Growth Des.*, 2009, **9**, 4834–4839.
17 J. P. Armstrong, C. Hurst, R. G. Jones, P. Licence, K. R. J. Lovelock, C. J. Satterley and I. J. Villar-Garcia, *Phys. Chem. Chem. Phys.*, 2007, **9**, 982–990.
18 K. R. J. Lovelock, A. Deyko, P. Licence and R. G. Jones, *Phys. Chem. Chem. Phys.*, 2010, **12**, 8893–8901.
19 Y. U. Paulechka, A. V. Blokhin, G. J. Kabo and A. A. Strechan, *J. Chem. Thermodyn.*, 2007, **39**, 866–877.
20 J. Troncoso, C. A. Cerdeiriña, Y. A. Sanmamed, L. Romaní and L. P. N. Rebelo, *J. Chem. Eng. Data*, 2006, **51**, 1856–1859.
21 D. H. Zaitsau, G. J. Kabo, A. A. Strechan, Y. U. Paulechka, A. Tschersich, S. P. Verevkin and A. Heintz, *J. Phys. Chem. A*, 2006, **110**, 7303–7306.
22 S. P. Verevkin, D. H. Zaitsau, V. N. Emel'yanenko, R. V. Ralys, A. V. Yermalayeu and C. Schick, *Thermochim. Acta*, 2013, **562**, 84–95.
23 L. M. N. B. F. Santos, A. I. M. C. L. Ferreira, V. Štejfa, A. S. M. C. Rodrigues, M. A. A. Rocha, M. C. Torres, F. M. S. Tavares and F. S. Carpinteiro, *J. Chem. Thermodyn.*, 2018, **126**, 171–186.
24 Y. U. Paulechka, D. H. Zaitsau, G. J. Kabo and A. A. Strechan, *Thermochim. Acta*, 2005, **439**, 158.
25 D. H. Zaitsau, N. Plechkova and S. P. Verevkin, *J. Chem. Thermodyn.*, 2019, **130**, 204–212.
26 A. R. West, *Solid state chemistry and its applications*, Wiley, New York, 1984.
27 X. Han, J. Ke, N. Suleiman, W. Levason, D. Pugh, W. Zhang, G. Reid, P. Licence and M. W. George, *Phys. Chem. Chem. Phys.*, 2016, **18**, 14359–14369.
28 Y. U. Paulechka, G. J. Kabo, A. V. Blokhin, A. S. Shaplov, E. I. Lozinskaya, D. G. Golovanov, K. A. Lyssenko, A. A. Korlyukov and Y. S. Vygodskii, *J. Phys. Chem. B*, 2009, **113**, 9538.
29 S. Vyazovkin, *Int. J. Chem. Kinet.*, 1996, **28**, 95–101.